Diffractive Optical Neural Networks

Minhan Lou and Weilu Gao*

Abstract Replacing the conventional imaging optics in machine vision systems with diffractive optical neural networks (DONNs) that leverage spatial light modulation and optical diffraction have been promising to enable new machine learning intelligence and functionality in optical domain, and reduce computing energy and resource requirements in electrical domain. In this chapter, the fundamental models to describe and design DONNs are first reviewed. Passive DONNs systems operating in the terahertz and short wavelength ranges are then introduced. Moreover, the advanced architectures that are resilient to hardware imperfections, that demonstrate improved performance, and that are implemented in photonic integrated circuits are discussed. Furthermore, the implementations of system reconfigurability through hybrid optoelectronic approaches are described. In addition, the effects from the physical model inaccuracy and how physics-aware training is used to correct deployment errors from both models and hardware are discussed. Finally, an all-optical reconfigurable DONNs system based on cascaded liquid-crystal spatial light modulators is demonstrated.

Keywords: forward and backward propagation models; terahertz; short wavelength; multichannel; multiplexing; metamaterials; photonic integrated circuits; spatial light modulator; hybrid optoelectronic reconfigurability; model inaccuracy; physics-aware training; all-optical reconfigurability

Minhan Lou
Department of Electrical and Computer Engineering, The University of Utah, e-mail: minhan.lou@utah.edu

Weilu Gao
Department of Electrical and Computer Engineering, The University of Utah, e-mail: weilu.gao@utah.edu

1 Introduction

Machine learning (ML) algorithms have seen unprecedented performance not only in imaging science and technology, including computer vision and autonomous driving [1, 2, 3], but also in broad scientific domains, such as the discovery of materials and molecules [4, 5] and chip and circuit design [6]. However, the execution of ML algorithms on hardware requires substantial computational and memory resources and consumes substantial energy. With the end of Dennard scaling and Moore's law, the energy consumption and integration density of electronic circuits have started to hit a bottleneck of further reducing the energy consumption and increasing the integration density of electronic circuits for processing trillions of operations [7, 8], which thus urgently calls for new high-throughput and energy-efficient hardware ML accelerators. Recently, optical architectures are emerging as high-performance ML hardware accelerators by leveraging fundamentally different particles, photons, to break the electronic bottleneck thanks to the extreme parallelism from the weak interaction and multiplexing of photons as well as low static energy consumption [9]. In addition to the demonstrations of two-dimensional (2D) integrated optical ML circuits [10, 11, 12, 13, 14], three-dimensional (3D) free-space optical systems exploit the out-of-plane light routing and can host millions of compact active devices [15, 16, 17, 18, 19, 20, 21, 22, 23, 24, 25, 26, 27, 28].

Among these demonstrations, diffractive optical neural networks (DONNs) can optically perform ML tasks through the *spatial light modulation* and *optical diffraction* of coherent light in multiple diffractive layers (Fig. 1a). Specifically, spatial light modulation on each diffractive layer regulates the amplitude and phase of input electric field, and optical diffraction creates interconnects between diffractive layers, which mimic deep neural network architectures. In order to perform ML tasks, amplitude and phase values in all diffractive layers are optimized so that coherent input images (e.g., Modified National Institute of Standards and Technology (MNIST) handwritten digit images) can be converged to one of predefined regions on a detector array that represents the label in supervised learning (e.g., numbers). The classification criterion is thus to find the detector region with the largest signal. Figure 1b displays an illustration that an input image with a handwritten digit 5 passes through multiple diffractive layers and then is focused onto one predefined region representing number 5. Replacing the conventional imaging optics in machine vision systems with DONNs can reduce the computational complexity and resource requirement on backend electronic processing units, and can bring new functionality to low-resolution imaging systems [29].

This chapter reviews the fundamentals and current development of free-space DONNs and is organized as follows. Section 2 describes the mathematical descriptions of DONNs and how the widely used backpropagation algorithm in ML is utilized for training and optimizing the parameters of diffractive layers. Section 3 discusses the pioneering hardware implementations of DONNs in the terahertz (THz) wavelength range, which benefit from the easy fabrication of diffractive layers. Section 4 further describes the DONNs in more accessible short wavelength ranges, where optical and optoelectronic components are mature. Section 5 summarizes a

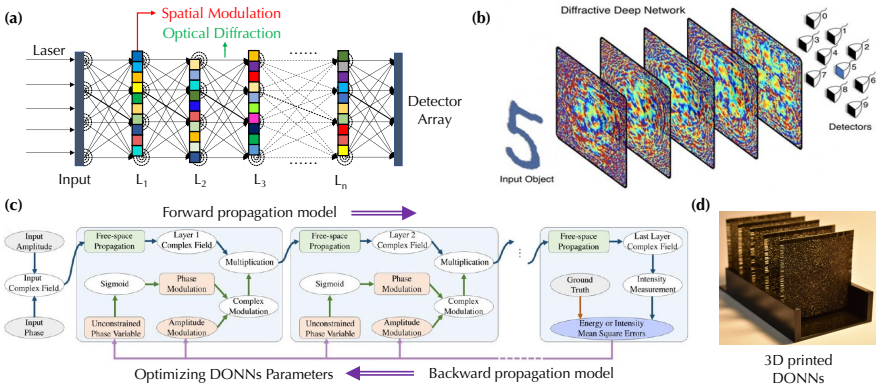

Fig. 1 Overview and the first demonstration of a THz DONNs system. (a) Schematic and (b) 3D illustration of a DONNs system. (c) Diagram of a DONNs model. Adapted from Ref. [30]. (d) A THz DONNs system implemented with 3D printing technology. (b) and (d) are adapted by permission from Dr. Aydogan Ozcan group from University of California, Los Angeles, U.S.A.

few advanced architectures with multiple hardware channels and optical multiplexing for high-performance and multifunctional DONNs. Section 6 discusses a few on-chip DONNs implemented in photonic integrated circuits in the telecommunication wavelength range. Section 7 describes reconfigurable hybrid DONNs with electronic systems. Section 8 discusses the discrepancies between physical models and hardware systems and how physics-aware training can mitigate them. Section 9 describes our latest demonstration of an all-optical reconfigurable DONNs with physics-aware modeling and training and without any intermediate electrical-optical conversions. Section 10 summarizes this chapter.

2 Fundamentals of DONNs

Figure 1c shows a detailed description of building blocks in a DONNs system illustrated in Fig. 1a. Input images are generated by shining coherent light, which mathematically correspond to complex-valued tensors. As input images propagate toward the detector array, which is called *forward propagation*, the input complex-valued tensors go through two fundamental operations. One is the free-space diffractive propagation and the other is the pixel-wise complex-valued multiplication when transmitting through diffractive layers. Both are included in the forward propagation model of a DONNs system as described in Section 2.1. The obtained images on the detector plane after forward propagation are generally different from desired output images. A loss function to quantify such difference, such as mean square error and cross entropy, is defined. The spatial light modulation parameters on diffractive layers are optimized to minimize the loss function, which is called *backward propagation*. Since the mathematical operations of DONNs are naturally tensor operations, the

state-of-the-art ML framework and hardware, such as PyTorch and general-purpose graphics processor units (GPUs), can be leveraged to substantially accelerate the optimization process, which is described in Section 2.2.

2.1 Forward propagation model

The optical diffraction is described by a shift-invariant Dyadic green's function, which can be approximated by Rayleigh-Sommerfeld diffraction equation

$$\begin{aligned} w(\mathbf{r}) &= \frac{z}{r^2}\left(\frac{1}{2\pi r} + \frac{n}{j\lambda}\right)\exp\left(\frac{j2\pi nr}{\lambda}\right) \\ \text{with } \mathbf{r} &= (x, y, z),\ r = \sqrt{x^2 + y^2 + z^2}, \end{aligned} \tag{1}$$

where n and λ are the refractive index of light propagation medium ($n = 1$ for air) and the wavelength, respectively. The diffraction filed $E_{\text{diff},m}$ from the transmitted field E_m^t of the m-th diffractive layer on the surface A_m is

$$E_{\text{diff},m}(\mathbf{r}) = \iint_{A_m} w(\mathbf{r} - \mathbf{r}')E_m^t(\mathbf{r}')ds'. \tag{2}$$

If the field is assumed to be uniform over each pixel with area S and the spatial sampling is adequate, the input field $E_{i,m+1}$ of the i-th pixel on the $(m+1)$-th layer from the diffraction of transmitted field E_m^t on the m-th layer can be expressed as

$$\begin{aligned} E_{i,m+1} &= E_{\text{diff},m}(\mathbf{r}_{i,m+1}) \\ &\approx \sum_k w(\mathbf{r}_{i,m+1} - \mathbf{r}_{k,m}) \iint_{A_{k,m}} E_m^t(\mathbf{r}_{k,m})ds' \\ &= \sum_k S \cdot w(\mathbf{r}_{i,m+1} - \mathbf{r}_{k,m})E_{k,m}^t \\ \text{with } E_{i,m}^t &= E_m^t(\mathbf{r}_{i,m}), \end{aligned} \tag{3}$$

where $\mathbf{r}_{i,m}$ is the position vector of the i-th pixel on the m-th layer.

Regarding the spatial light modulation, the optical response of each pixel is assumed to be that from the periodic array of that pixel under uniform illumination, which is

$$\begin{aligned} E_{i,m+1} &= \textstyle\sum_k C_{i,k,m}E_{k,m}^t \\ &= \textstyle\sum_k C_{i,k,m}t_{k,m}E_{k,m} \\ \text{with } C_{i,j,m} &= S \cdot w(\mathbf{r}_{i,m+1} - \mathbf{r}_{j,m}), \end{aligned} \tag{4}$$

where $t_{i,m}$ is the complex-valued transmission coefficient of the i-th pixel on the m-th layer. The detectors on the layer D only capture light intensity $I_{i,D}$ as $|E_{i,D}|^2$.

Since the diffraction equation (Eq. 2) is shift-invariant, the convolution theorem and Fast Fourier Transform (FFT) can be utilized to substantially speed-up the calculation of Eq. 4, which is the most computationally intensive in DONNs models. The computation complexity of the direct summation in Eq. 4 for $N \times N$ pixels is $O(N^4)$, which is reduced to $O(N^2 \log(N))$ through FFT.

2.2 Backward propagation model

The training or optimization of diffractive layers for a fixed single pair of input and output images can be done with the Gerchberg-Saxton (GS) algorithm, which has been a standard approach for hologram design [31]. However, the iterative nature of GS algorithm makes it difficult to be modified for the training with a large number of input images and optimization parameters, which is ubiquitous in ML tasks. Backpropagation algorithm, where the gradient propagates according to chain rules and along the descent direction, has been a widely used efficient ML training approach [32]. According to Eq. 4 and a loss function $\mathcal{L}$, the gradients with respect to the field can be calculated recursively from the final layer to the first layer as

$$\begin{aligned} \left.\frac{\partial \mathcal{L}}{\partial E_{k,m}}\right|_{m<D} &= \sum_j \frac{\partial \mathcal{L}}{\partial E_{j,m+1}} \frac{\partial E_{j,m+1}}{\partial E_{k,m}} \\ &= \sum_j \frac{\partial \mathcal{L}}{\partial E_{j,m+1}} C_{j,k,m} t_{k,m}. \end{aligned} \tag{5}$$

The gradients with respect to the diffractive layer parameters of the m-th layer can be calculated as

$$\begin{aligned} \frac{\partial \mathcal{L}}{\partial t_{i,m}} &= \sum_k \frac{\partial \mathcal{L}}{\partial E_{k,m}} \frac{\partial E_{k,m}}{\partial t_{i,m}} \\ &= \sum_k \frac{\partial \mathcal{L}}{\partial E_{k,m}} C_{k,i,m} E_{i,m-1}. \end{aligned} \tag{6}$$

Nowadays, the PyTorch (version $>$ 1.8) ML framework has provided fast and efficient computation of FFT and its gradient backpropagation, which can substantially speed-up the calculations of forward the backward propagation models in DONNs.

3 Terahertz-wavelength DONNs

Mature 3D printing technologies have enabled precise and versatile manufacturing of diffractive optical components in long-wavelength ranges. With such capability, Lin et al. have implemented the first hardware DONNs system in the terahertz

(THz) wavelength range [15]. Figure 1d shows the fabricated five-layer THz DONNs system illuminated by a coherent THz source. Each diffractive layer consists of 200×200 pixels in an $8 \times 8\,\mathrm{cm}^2$ area. As described before, this system can perform image classification tasks in the MNIST and Fashion-MNIST datasets with good classification accuracies. Once the diffractive layers are fabricated, the inference of ML tasks using this system does not consume energy. In addition, such inference is performed in a single-clock-cycle forward propagation at the light speed. Thus, the implemented THz DONNs system is an energy-efficient and high-throughput ML inference hardware accelerator. In each diffractive layer, each pixel is assumed to possess the phase-only transmission response, which is directly correlated with the pixel height through a simple relationship between the phase delay and plane wave propagation distance. By defining the loss function and employing the backpropagation algorithm described in Section 2, the optimized phase values of pixels in diffractive layers can be obtained and these diffractive layers can be fabricated with corresponding pixel heights using 3D printers.

The THz DONNs system is trained as an image classifier to perform automated classification of handwritten digits from 0 to 9 in the MNIST dataset. Input images are binary encoded by letting the input THz light pass through the metal plates with engraved hollow digits from input images. The loss function is minimized to maximize the optical signal for desired detector region for accurate classification. The calculated test classification accuracy is 91.75 % and the experimental one from selected 50 images is 88 %. Furthermore, deep architectures with more diffractive layers are shown to be better in classification accuracies than those with less diffractive layers, suggesting that DONNs exhibit "depth" advantages despite without nonlinear functions.

However, the performance of DONNs is generally vulnerable to hardware imperfection. One strategy to construct imperfection-resilient DONNs is to incorporate the modeled imperfection into the training process. For example, the classification accuracies of THz DONNs are sensitive to the translation, scaling, and rotation of input images, which are inevitable in practical systems and machine vision applications. In order to construct DONNs systems that are resilient to these object transformations, Mengu et al. first quantify the sensitivity of DONNs to these uncertainties as shown in Fig. 2a and further develop a training strategy that incorporates the formulated input object translation, scaling, and rotation as uniformly distributed random variables [33]. As a result, this training approach successfully guides the optimization of diffractive layers toward a shift-, scale-, and rotation-invariant solution. Furthermore, Mengu et al. model layer-to-layer misalignments as random variables and introduce them in the training process to train vaccinated DONNs to be robust against 3D misalignments, while at the cost of reduced classification accuracy [34].

Another strategy to improve the robustness of DONNs systems is to explore different architectures with reduced complexity. Li et al. propose a robust multiscale diffractive U-Net (MDUNet) DONNs framework by introducing sampling and skip connections [35]. Instead of having high pixel resolution for each diffractive layer, the sampling processes, including downsampling and upsampling, change the pixel size and resolution as shown in Fig. 2b. The sampling module can greatly improve

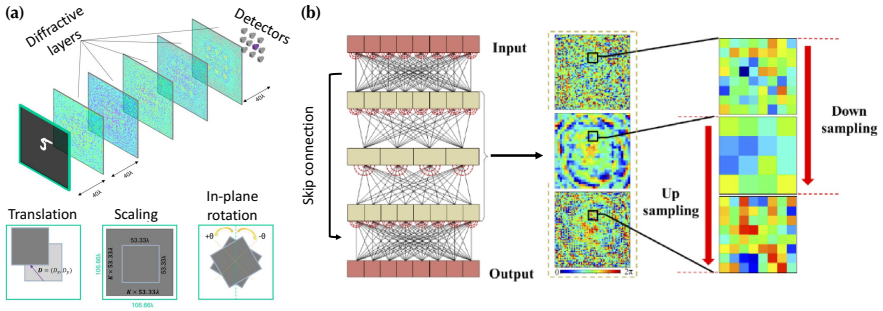

Fig. 2 Hardware-imperfection resilient DONNs. (a) Translation, scaling, and rotation of input images in DONNs. Adapted by permission from American Chemical Society: ACS Photonics, Scale-, Shift-, and Rotation-Invariant Diffractive Optical Networks, Mengu, D. et al., © 2020. (b) Schematic of the MDUNet architecture, and downsampling and upsampling principles. Adapted under the terms of the Optica Open Access Publishing Agreement from Optica Publishing Group: Optics Express, Multiscale diffractive U-Net: a robust all-optical deep learning framework modeled with sampling and skip connections, Li, Y. et al., © 2022.

the system robustness by reducing the complexity of diffractive layers. Furthermore, the skip connections can fusion the multiscale features from diffractive layers with various resolution, which can achieve the similar performance compared to cascaded fully connected DONNs while with reduced model parameters.

4 Short-wavelength DONNs

The practical technologies for generating, manipulating, and detecting THz electromagnetic radiations are limited. This has been widely recognized as the THz gap, meaning that efficient and feasible THz components are challenging to be implemented using either electronic or optical approaches [36]. As a result, the implementation of such THz DONNs systems requires special, costly, and sophisticated equipment. Moreover, there is a vast majority of imaging applications in shorter wavelengths, including visible and near-infrared wavelengths. Thus, it is essential to extend the operation of DONNs to these wavelengths. In addition to more accessible optical hardware in these wavelengths, compact and advanced diffractive components, such as metasurfaces, can be incorporated [37].

Short visible wavelengths, on the order of hundreds of nanometers, require modern nanofabrication technologies to manufacture diffractive layers. As shown in Fig. 3a, Chen et al. employ a multi-step photolithography-etching process to produce five diffractive layers on SiO_2 substrates and construct a visible-wavelength DONNs classifier at a single wavelength 632.8 nm to recognize original images of handwritten digits in the MNIST dataset and modified images that are covered or altered [38]. The calculated classification accuracy is 91.57 % and the experimental accuracy is 84 %. Moreover, Goi et al. utilize galvo-dithered two-photon nanolithography

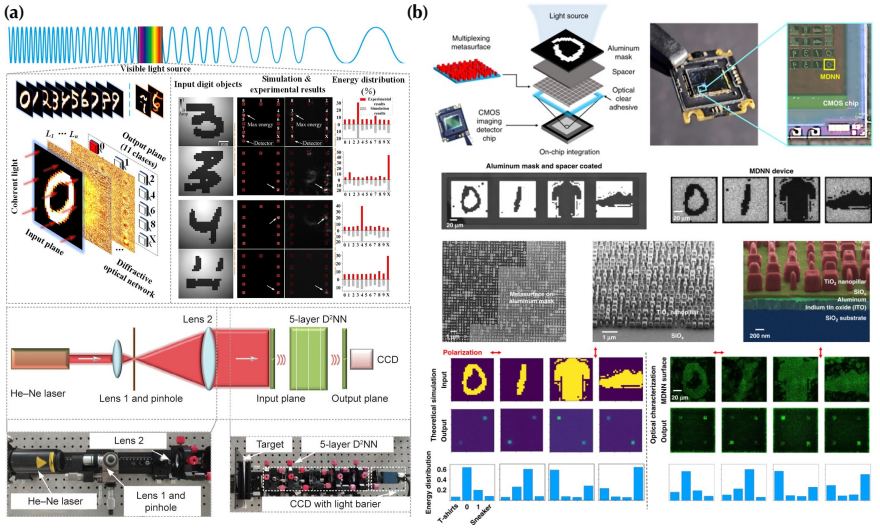

Fig. 3 DONNs in visible wavelengths. (a) Schematic diagram and experimental setup of the visible-light DONNs system for the classification of MNIST images. Adapted under a Creative Commons license CC BY-NC-ND 4.0 from Elsevier: Engineering, Diffractive Deep Neural Networks at Visible Wavelengths, Chen, H. et al., © 2021. (b) Experimental demonstration of multiplexed metasurface-enabled on-chip DONNs. Adapted under a Creative Commons Attribution 4.0 International License from Springer Nature: Light: Science & Applications, Metasurface-enabled on-chip multiplexed diffractive neural networks in the visible, Luo, X. et al., © 2022.

with axial nanostepping of 10 nm to achieve a pixel density of $> 5 \times 10^6\,\mathrm{mm}^{-2}$ in diffractive layers [39], which are further integrated with complementary metal-oxide semiconductor (CMOS) chips for optical decryptors in the near-infrared range.

Furthermore, Luo et al. employ metasurfaces that consist of subwavelength rectangular TiO_2 nanopillars in diffractive layers and demonstrate a multiplexed metasurface-based DONNs system integrated with a CMOS imaging sensor for a chip-scale architecture, which can process information directly at physical layers for energy-efficient and ultra-fast image processing in the visible range [40]; see Fig. 3b. Metasurfaces consisting of subwavelength resonators can manipulate the wavefront of light in nearly arbitrary manners and have enabled high-efficiency and broadband holograms [41] and the miniaturized systems to perform mathematical operations [42], such as differentiation [43, 44] and convolution [45]. Due to the compact and thin characteristics of metasurfaces, Luo et al. achieve a pixel areal density up to $6.25 \times 10^6\,\mathrm{mm}^{-2}$ multiplied by the number of channels, highlighting a significant contrast to the THz DONNs system with a low pixel density $6.25\,\mathrm{mm}^{-2}$ [15]. The multiplexing feature is discussed in Section 5.2.

5 Advanced DONNs architectures

The state-of-the art convolutional neural networks in electronic systems can achieve the MNIST classification accuracy > 99.9 % [46]. Despite the promising capabilities in demonstrated DONNs, there is a noticeable gap of the classification accuracy between DONNs and their electronic counterparts. In addition, one DONNs system is typically designed for only one specific ML task. This section summarizes a few recent efforts of exploring advanced DONNs architectures with improved performance and expanded functionalities.

5.1 Multichannel DONNs

One reason why DONNs underperform is due to the limitation that detectors can only capture nonnegative real-valued light intensity without phase information. To mitigate this constraint, Li et al. propose a differential measurement technique shown in Fig. 4a [47]. Each class is assigned to a pair of detectors and the largest pair reading difference is the classification criterion and training target. Moreover, divided individual classes in a target dataset are processed with two jointly trained DONNs in parallel, which can achieve the calculated classification accuracies of 98.52 %, 91.48 %, and 50.82 % for MNIST, Fashion-MNIST, and grayscale CIFAR-10 datasets, respectively. These values are close to those obtained in some all-electronic deep neural networks, such as LeNet, which achieves 98.77 %, 90.27 %, and 55.21 % for the same datasets, respectively.

Furthermore, Rahman et al. propose the approach of using feature engineering and ensemble learning with multiple independently trained diffractive layers to substantially improve the classification performance of DONNs [48]. A set of input filters are first utilized to extract features from preprocessed input images and each feature image passes through a DONNs system with differential detection scheme, as shown in Fig. 4b. With carefully selected ensemble of DONNs, this approach can achieve an classification accuracy of CIFAR-10 images as 62.13 ± 0.05 %, which demonstrate an accuracy improvement of > 16 % compared to the average performance of the individual DONNs.

The DONNs systems we have discussed so far are purely passive. Thus, deploying different ML tasks requires the complete rebuilding of the entire system, which substantially degrades the hardware utilization efficiency. Li et al. propose a multitask learning DONNs architecture in Fig. 4c, which can automatically recognize which task is being deployed in real-time and perform corresponding classification task [49]. Instead of constructing two separate DONNs systems for the image classifications in the MNIST and Fashion-MNIST datasets, a few diffractive layers are shared and two split branches of diffractive layers are tailored for these two different but related ML tasks. The loss function regularization is employed in the training process to balance the performance of each task and prevent overfitting. The numerical calculation results demonstrate that the multitask DONNs system can achieve the same accuracy

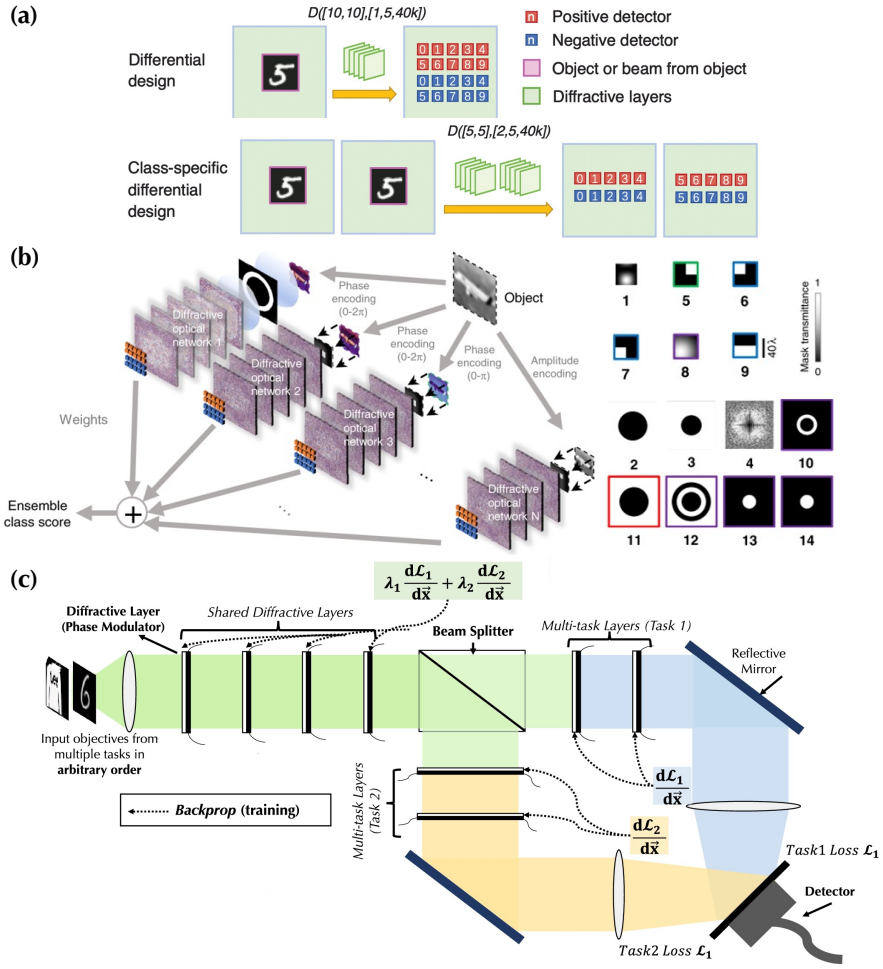

Fig. 4 Multichannel DONNs. (a) Illustration of differential and class-specific differential DONNs systems. Adapted under a Creative Commons Attribution 4.0 Unported License from SPIE: Advanced Photonics, Class-specific differential detection in diffractive optical neural networks improves inference accuracy, Li, J. et al., © 2019. (b) An ensemble of DONNs systems consisting of multiple different DONNs systems with the features of input images engineered by a set of input filters before each DONNs system that forms the ensemble. Adapted under a Creative Commons Attribution 4.0 International License from Springer Nature: Light: Science & Applications, Ensemble learning of diffractive optical networks, Rahman, M.S.S. et al., © 2021. (c) Illustration of a multitask DONNs architecture with two image classification tasks deployed. Adapted under a Creative Commons Attribution 4.0 International License from Springer Nature: Scientific Reports, Real-time multi-task diffractive deep neural networks via hardware-software co-design, Li, Y. et al., © 2021.

for both tasks compared to two separate DONNs while with $> 75\,\%$ improvement in hardware utilization efficiency.

5.2 Multiplexing DONNs

In addition to introducing multiple hardware channels, including detector channels and multiple optical paths, as summarized in Section 5.1, the intrinsic physical features of optical electromagnetic waves, such as polarization and wavelength, can enable parallel processing with multiplexing and thus boost the performance and functionalities of DONNs systems.

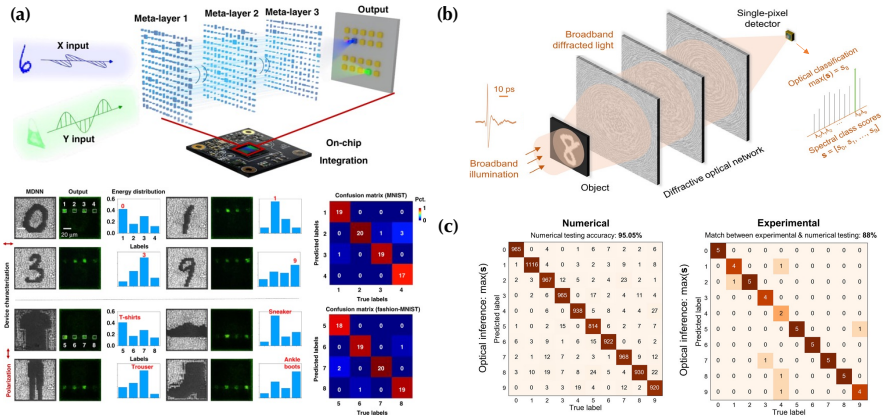

Fig. 5 Multiplexing DONNs. (a) Metasurface-enabled polarization-multiplexed DONNs system for two classification tasks. Adapted under a Creative Commons Attribution 4.0 International License from Springer Nature: Light: Science & Applications, Metasurface-enabled on-chip multiplexed diffractive neural networks in the visible, Luo, X. et al., © 2022. (b) Schematic of spectral encoding of spatial information for object classification, and (c) experimentally measured and the numerically calculated optical power spectra and classification confusion matrices of MNIST images with a single-pixel detector. (b) and (c) are adapted under a Creative Commons Attribution License 4.0 from American Association for the Advancement of Science: Science Advances, Spectrally encoded single-pixel machine vision using diffractive networks, Li, J. et al, © 2021.

For example, the metasurfaces developed by Luo et al. can enable not only visible-wavelength compact integrated DONNs as discussed in Section 4 but also the polarization-multiplexing capability. The rectangular cross-section of subwavelength TiO_2 nanopillars produces different effective refractive indices along the two crossed axes, which is the fundamental mechanism for polarization multiplexing. These two orthogonal polarization channels are utilized to experimentally construct a multitask DONNs system for the simultaneous recognition of input images from the MNIST and Fashion-MNIST datasets, as shown in Fig. 5a. Furthermore, Li et al. propose a polarization-multiplexed diffractive processor to all-optically per-

form multiple arbitrarily-selected linear transformations by inserting an array of linear polarizers with predetermined orientations in the middle of trainable isotropic diffractive layers [50].

The multiplexing technique can also lower the requirement of hardware resource, which is particularly crucial for technically challenging THz wavelength range. For example, instead of assigning class in the detector array, Li et al. utilize a broadband THz illumination to assign each digit/class in the MNIST dataset to 10 wavelengths [51]. Thus, only a single-pixel detector is needed at the output end as shown in Fig. 5b. Furthermore, the calculated classification accuracy is $> 95\,\%$ and the experimentally obtained classification accuracy using 50 images is 88 %, as shown in the confusion matrices in Fig. 5c.

6 DONNs in photonic integrated circuits

Although DONNs are mainly implemented in free space, there have been recent efforts of creating on-chip DONNs in 2D silicon photonic integrated circuits (PICs). The compact footprint, lithography-defined optical alignment, and CMOS-compatible and mass manufacturing of silicon PICs make a promising platform for miniaturized DONNs systems.

Zarei et al. propose an integrated on-chip five-layer DONNs consisting of five one-dimensional (1D) metalines at a telecommunication wavelength of $1.55\,\mu$m [52]. Each element in a metaline is an etched rectangle slot with subwavelength dimensions on a silicon-on-insulator substrate, which diffracts the in-plane propagating optical waves. Thus, a metaline behaves like a 1D-version diffractive layer in a free-space DONNs system. A 2D input image is flattened to a 1D array and a 1D on-chip detector array is utilized to capture output signals. Wang et al. later experimentally implement such a system as illustrated in Fig. 6a [53]. The chip contains $\sim 10^3$ nanoscale diffractive etched slot elements in a $0.135\,\text{mm}^2$ area. The test images are three binary letters "X", "Y", and "Z" with random amplitude and phase noises, which are encoded and coupled into the chip through an array of grating couplers. As light propagates through multiple metalines or metasurfaces, three detector channels at the output end represent the class of input images and picking up the largest detector signal among three channels is the classification criterion, as shown in Fig. 6b. Figure 6c displays the confusion matrices obtained from numerical finite-difference-time-domain (FDTD) simulations, continuous-wave (CW) excitation, and pulsed excitation, which have the classification accuracies of 96 %, 92 %, and 89 %, respectively.

Furthermore, Zhu et al. experimentally demonstrate a more compact integrated DONNs shown in Fig. 6d [54]. The ultracompact diffractive cell is a 10-input-10-output multimode interferometer. The input image encoding and nonlinear activation functions are implemented by a mesh of electrically-controllable Mach-Zehnder interferometers (MZIs) with thermal-optic phase shifters, as well as detectors. The number of phase shifters, which determines the footprint and energy consumption

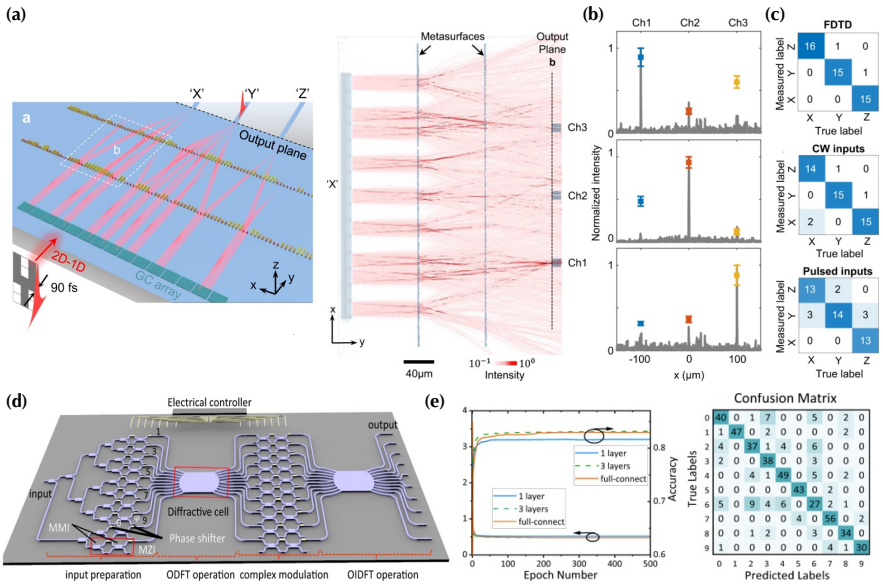

Fig. 6 DONNs in photonic integrated circuits. (a) Schematic and in-plane field distribution of the integrated DONNs system with on-chip diffractive metasurfaces. (b) Comparison of measured optical intensities (dots with error bars) and the simulated optical distribution (gray curve) on the output plane. (c) Confusion matrices obtained from FDTD simulations, as well as CW and pulse light excitation. (a), (b), and (c) are adapted under a Creative Commons Attribution 4.0 International License from Springer Nature: Nature Communications, Integrated photonic metasystem for image classifications at telecommunication wavelength, Wang Z. et al., © 2022. (d) Schematic of an experimental on-chip space-efficient DONNs device. (e) The numerical testing results of accuracy and loss versus epoch number for the Fashion-MNIST dataset and the experimentally obtained confusion matrix. (d) and (e) are adapted under a Creative Commons Attribution 4.0 International License from Springer Nature: Nature Communications, Space-efficient optical computing with an integrated chip diffractive neural network, Zhu H.H. et al., © 2022.

of the whole chip, scales linearly with the input data dimension. The calculated and experimentally obtained classification accuracies for the MNIST dataset are 92.6 % and 91.4 %, respectively. These two values for the Fashion-MNIST dataset are 81.4 % and 80.4 % as shown in Fig. 6e.

7 Reconfigurable hybrid DONNs

We have so far mainly focused on passive DONNs, in which the spatial light modulation responses of diffractive layers are fixed once they are fabricated. Thus, the fabricated passive DONNs system can only be utilized for a specific ML task. Although multitasking and multiplexing architectures described in Section 5 can handle a few but still limited tasks, it is more desirable to be able to dynamically adjust

the response of diffractive layers for *reconfigurable* DONNs systems. The central component for such implementation is a spatial light modulator (SLM), which can regulate the amplitude and phase of the free-space propagating wavefront under the control of external stimulus.

Figure 7a summarizes a few free-space all-optical and hybrid optoelectronic computing paradigms, which can potentially achieve reconfigurability [55]. Scheme (i) represents all-optical DONNs as we have discussed in prevision sections. Scheme (ii) represents a canonical $4f$ Fourier imaging processing system, where a diffractive layer spatially modifies the wavefront. The output image is further processed through electronic neural networks for performing ML tasks. Scheme (iii), which is similar to Scheme (ii), further removes any diffractive layer and relies only on the free-space propagation for photonic extreme ML [56]. In Schemes (i) to (iii), the encoding method of input images is fixed. Instead, Wu et al. propose Scheme (iv) that electronic neural networks are trained to encode input images so that the optical free-space propagation can perform ML tasks [55]. Schemes (ii) to (iv) are hybrid optoelectronic systems and the reconfigurability can be implemented by updating electronic systems. However, strictly speaking, these are not reconfigurable optical systems. Miscuglio et al. experimentally demonstrate some level of optical reconfigurability in Scheme (ii) as shown in Fig. 7b [57]. Specifically, a digital micromirror device (DMD), which is one type of SLM for amplitude-only modulation, is used as a diffractive layer. The electronic system is trained to perform ML tasks by reading out images captured by the camera and sending the control signal to DMD. The experimental results show the classification accuracies of 98 % for the MNIST dataset and 54 % for the CIFAR-10 dataset. However, the computation is still heavily performed in the electrical domain, which significantly compromises the advantages of optical computing such as high energy efficiency and parallelism.

Zhou et al. have demonstrated a major advance of implementing large-scale reconfigurable DONNs by replacing diffractive layers shown in Scheme (i) of Fig. 7a with an electrically-controllable liquid-crystal SLM [58]. Specifically, the authors construct a reconfigurable diffractive processing unit (DPU) consisting of a DMD, a phase-only SLM, and a CMOS detector, as shown in Fig. 7c. The DMD encodes input images; the SLM is a reconfigurable diffractive layer; and the CMOS reads out the output image to the electrical domain. Multiple DPU blocks can be utilized to construct complex neural network architectures, such as a hybrid DONNs system shown in Fig. 7d. In contrast to all-optical DONNs, there are electrical-to-optical (E/O) and optical-to-electrical (O/E) conversions between layers. The CMOS readout from the DPU in the previous layer is electronically processed to control the DMD and SLM from the DPU in the next layer. In addition, nonlinear activation is applied during these E/O and O/E conversions. But the system reconfigurability is achieved by SLMs in the optical domain. Although the demonstrated system is still hybrid or optoelectronic, an advantage is its versatility to construct different architectures, such as diffractive recurrent neural networks (DRNNs) shown in Fig. 7e. However, the disadvantages from E/O and O/E conversions include increased energy consumption and processing latency, as well as the discrepancy between models and physical

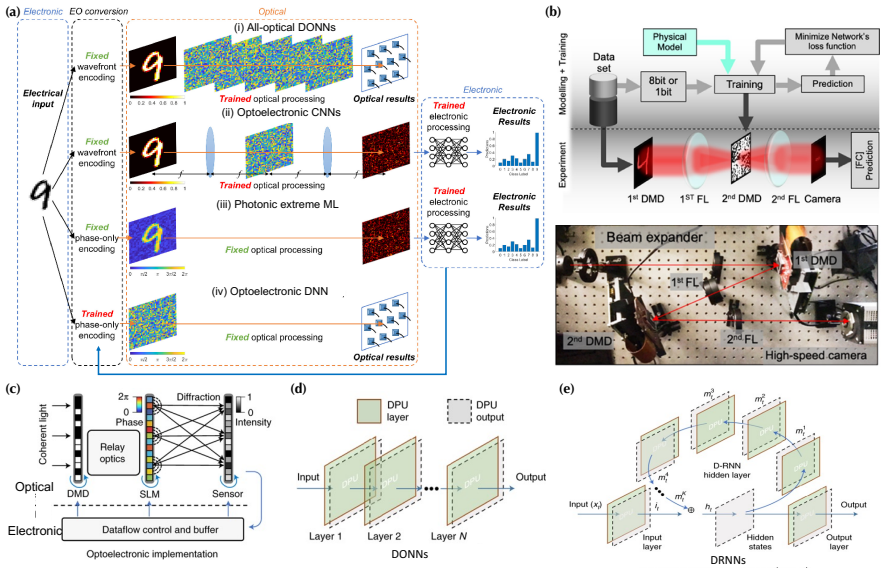

Fig. 7 Reconfigurable hybrid DONNs. (a) The computing paradigms of all-optical and hybrid optoelectronic neural network. Adapted under the terms of the Optica Open Access Publishing Agreement from Optica Publishing Group: Optics Express, Only-train-electrical-to-optical-conversion (OTEOC): simple diffractive neural networks with optical readout, Wu, L. et al., © 2022. (b) Schematic and photo of a hybrid optoelectronic Fourier neural network experimental setup. Adapted under the terms of the Optica Open Access Publishing Agreement from Optica Publishing Group: Optica, Massively parallel amplitude-only Fourier neural network, Miscuglio, M. et al., © 2020. (c) Schematic of a DPU including a DMD, a phase-only SLM, and a CMOS sensor. Two neural network architectures constructed using DPUs including (d) DONNs and (e) DRNNs. (c), (d), and (e) are adapted by permission from Springer Nature: Nature Photonics, Large-scale neuromorphic optoelectronic computing with a reconfigurable diffractive processing unit, Zhou, T. et al., © 2021.

systems, which limits the reconfigurability. The model inaccuracy and physics-aware training for correction are discussed in Section 8.

8 Model inaccuracy and physics-aware training

In addition to hardware imperfection, there are always discrepancies between calculation models and hardware systems, which can also lead to the deployment errors of trained models to experimental systems. This section first describes our recent discovery of some origins of the model inaccuracy, which come from the over-simplification of the electromagnetic wave interaction and propagation in diffractive layers and free space in the analytical model described in Section 2.1. Although the hardware-imperfection training approaches described in Section 3 can provide some

model resilience, they are typically at the sacrifice of system performance. This section further introduces two physics-aware training frameworks to minimize the deployment errors from both models and hardware.

8.1 Model inaccuracy

The analytical model described in Section 2.1 does not consider any multiple reflection-diffraction effect circulating between diffractive layers as shown in Fig. 8a . Lou et al. incorporate this effect through transfer matrix method and iterative calculations as a modified trainable model. The DONNs system is trained with the MNIST dataset using the analytical model without reflection and the accuracy drops when the trained model is evaluated using the modified model with reflection. Figure 8b displays the accuracy drop as a function of a round-trip reflected energy ratio over the total energy (α_{RT}) for different trained diffractive masks with different material indices. The reflection effect is negligible with low-index materials such as 3D printing polymers with the refractive index ~ 1.7 in THz DONNs systems [15, 59]. However, it is substantial with high-index materials, which are generally involved in advanced DONNs. For example, the metasurfaces made of high-index dielectric materials can enable compact and high-density DONNs systems as described in Section 4. In addition, reconfigurable DONNs can be constructed with emerging chalcogenide phase change materials, which have THz indices > 10 [60] and visible-near-infrared indices > 3 [61]. Thus, it is crucial to consider reflection effect when developing next-generation compact and multifunctional DONNs.

In addition, Lou et al. analyze the interpixel interaction effect by comparing the classification accuracies obtained from the analytical model and full-wave FDTD simulations, which can precisely describe experiments [62]. For a two-layer DONNs system, Fig. 8c demonstrates that a high accuracy needs a large pixel complexity, which represents a fast-varying spatial response of trained diffractive layers. However, the large complexity leads to a low matching rate between the analytical model and FDTD simulations, which is because the pixel optical response is considerably affected by neighboring pixels and deviates from the periodic pixel assumption in the analytical model. Deep DONNs can help to break down such trade-off. As shown in Fig. 8d, the pixel complexity for a one-layer DONNs system is much larger than that in a five-layer DONNs system to achieve similar high classification accuracies. But the matching rate and thus experimental deployment of the five-layer DONNs system is better, highlighting the “depth” advantage in achieving high accuracy and accurate deployment simultaneously.

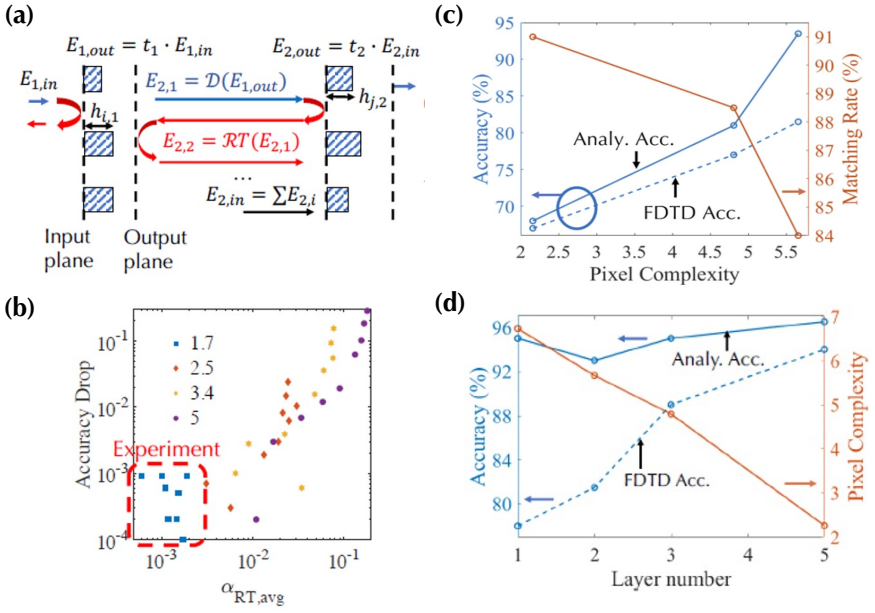

Fig. 8 Model inaccuracy. (a) Illustration of interlayer reflection effect. (b) Accuracy drop as a function of average round-trip power ratio $\alpha_{\mathrm{RT,\,avg}}$ for multiple trained diffractive masks with different refractive indices. (c) Classification accuracy obtained from analytical and FDTD approaches and their matching rate as a function of the pixel complexity of diffractive layers. (d) Classification accuracy obtained from the analytical model and FDTD simulations, as well as diffractive layer complexity as a function of depth. Adapted by permission from Optica Publishing Group: Optics Letters, Effects of interlayer reflection and interpixel interaction in diffractive optical neural networks, Lou, M. et al., © 2022.

8.2 Physics-aware training

As discussed before, both hardware-imperfection and model inaccuracy can lead to deployment errors. In order to correct these errors, the training processes incorporating hardware physics emerge as effective approaches. As shown in the flowchart in Fig. 9a, Zhou et al. develop an adaptive training approach to circumvent system deployment errors in their reconfigurable hybrid neural networks as discussed in Section 7 [58]. Specifically, the *in silico* trained model is deployed onto the practical system and the *in-situ* experimental outputs from each DPU CMOS sensor are utilized to update the trained model during the forward propagation. As shown in Fig. 9b, the direct deployment of trained model leads to a substantial accuracy drop because of the accumulated errors between models and physical systems as light propagates. In contrast, the adaptive training process successfully recovers a high accuracy. Furthermore, as illustrated in Fig. 9c, Wright et al. introduce a generic hybrid *in situ-in silico* physics-aware training algorithm that takes experimentally measured intermediate physical quantities during forward propagation (f_{p}) into the compu-

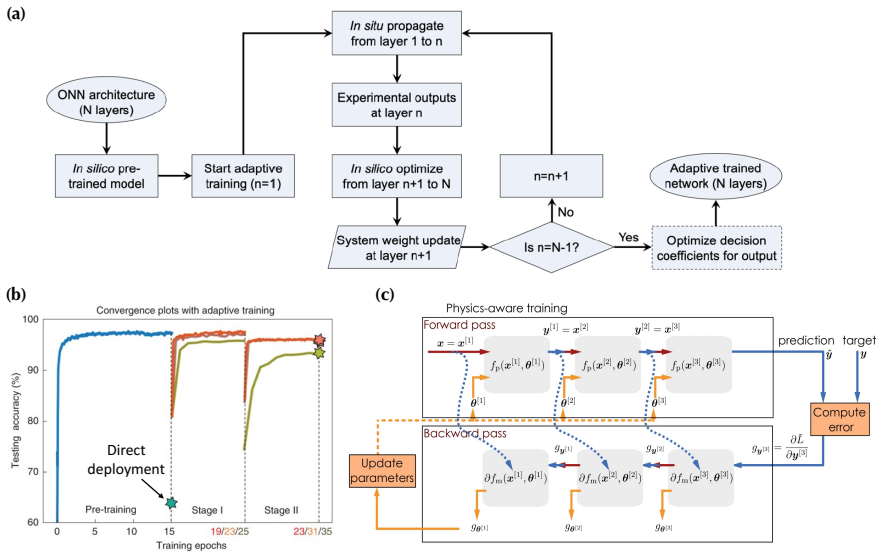

Fig. 9 Physics-aware training. (a) Flowchart of the proposed adaptive training approach. (b) Convergence plots of hybrid optoelectronic DONNs evaluated on the MNIST test dataset. The blue plot shows the pre-training process. Orange, brown and yellow plots represent the adaptive training with full, 20%, and 2% training sets, respectively. (a) and (b) are adapted by permission from Springer Nature: Nature Photonics, Large-scale neuromorphic optoelectronic computing with a reconfigurable diffractive processing unit, Zhou, T. et al., © 2021. (c) Schematic of the full training loop for the physics-aware training algorithm applied to arbitrary physical neural networks. f_{p} is the physical forward function, f_{m} is the approximate forward function in the mode, and $g_{\boldsymbol{\theta}}$ is the gradient of the loss function respect to parameter $\boldsymbol{\theta}$. Adapted under a Creative Commons Attribution 4.0 International License from Springer Nature: Nature, Deep physical neural networks trained with backpropagation, Wright, L.G. et al., © 2022.

tation of backpropagation gradients ($g_{\boldsymbol{\theta}}$) with the approximate model (f_{m}) [63]. This approach allows training any controllable physical systems, even when physical layers lack any mathematical isomorphism to conventional neural network layers.

9 All-optical reconfigurable DONNs

This section describes our latest demonstration of an all-optical reconfigurable DONNs system based on cascaded liquid-crystal SLMs as shown in Fig. 10a [64]. The system is exactly the fully reconfigurable version of Scheme (i) in Fig. 7a without any electrical-optical conversions. The fullstack implementation of software and hardware has considered the imperfections from both models and systems. Thus, the *in silico* trained model can be accurately deployed to the physical system without the need for further tuning. Specifically, the diffraction model is modified to be system-specific through a convolutional Fresnel method [65]. Furthermore, each liquid-

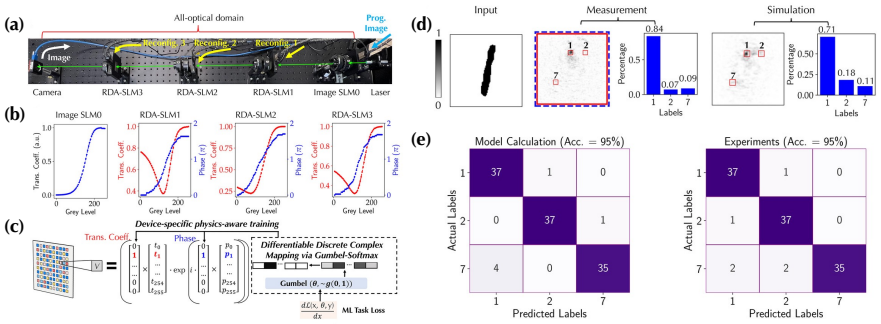

Fig. 10 All-optical reconfigurable DONNs. (a) A photo of the experimental system of all-optical reconfigurable DONNs. Reconfigurable diffractive layers (RDAs) are based on liquid-crystal SLMs. (b) The coupled amplitude and phase modulation responses for used SLMs. (c) Illustration of implementing differentiable discrete complex mapping via Gumbel-Softmax for device-specific physics-aware training. (d) An input image of a handwritten digit 1 from the MNIST dataset, experimentally measured diffraction pattern and corresponding intensity distribution, and calculated diffraction pattern and corresponding intensity distribution. (e) Confusion matrices of the computer-trained model and experimental measurement. Adapted by permission from Wiley: Laser & Photonics Reviews, Physics-Aware Machine Learning and Adversarial Attack in Complex-Valued Reconfigurable Diffractive All-Optical Neural Network, Chen, R. et al., © 2022.

crystal SLM has a coupled amplitude and phase modulation. Figure 10b displays experimentally measured nonmonotonic and coupled modulation curves under 256 discrete grey levels, which break down the backpropagation algorithm. In order to incorporate such device response, the authors develop a device-specific physics-aware training approach through differentiable discrete mapping based on the categorical reparameterization with Gumbel-Softmax, as illustrated in Fig. 10c. This approach can incorporate arbitrary device response. In addition, the full reconfigurability of this system enables fast and precise pixel-by-pixel optical alignment.

With the accurate diffraction calculation, device-specific physics-aware training, and precise hardware alignment, the trained gray levels of SLMs can be fast and precisely deployed on the experiment setup. The input images of three digits 1, 2, and 7 from the MNIST dataset are used for training. Figure 10d displays an excellent agreement between experimentally measured and calculated output images and corresponding optical intensity distribution. Furthermore, the confusion matrices and accuracies obtained from calculations and experiments in Fig. 10e also match well.

10 Summary

This chapter has described the fundamentals and current development of both passive and actively reconfigurable DONNs systems. Various implementations of diffractive layers at different wavelengths, such as THz and visible dielectric components,

compact and integrated metamaterials, and active spatial light modulators, as well as versatile system architectures have been proposed and experimentally demonstrated to enable high-performance and multifunctional DONNs systems. Furthermore, the deployment errors from hardware imperfections and models, as well as the training strategies to correct these errors have been introduced. We believe that the future development of DONNs systems will focus on reducing the footprint of individual diffractive pixels and overall architecture, and enhancing the capability of handling sophisticated ML tasks, which will require not only fast-computed, trainable, and accurate physical models but also new material platforms and their enabling innovative devices.

References

1. Y. LeCun, Y. Bengio, G. Hinton, Nature **521**(7553), 436 (2015). DOI https://doi.org/10.1038/nature14539
2. I. Goodfellow, Y. Bengio, A. Courville, Y. Bengio, *Deep learning*, vol. 1 (MIT press Cambridge, 2016)
3. S.P. Rodrigues, Z. Yu, P. Schmalenberg, J. Lee, H. Iizuka, E.M. Dede, Nat. Photonics **15**(2), 66 (2021). DOI https://doi.org/10.1038/s41566-020-00736-0
4. K.T. Butler, D.W. Davies, H. Cartwright, O. Isayev, A. Walsh, Nature **559**(7715), 547 (2018). DOI https://doi.org/10.1038/s41586-018-0337-2
5. A.W. Senior, R. Evans, J. Jumper, J. Kirkpatrick, L. Sifre, T. Green, C. Qin, A. Žídek, A.W. Nelson, A. Bridgland, et al., Nature **577**(7792), 706 (2020). DOI https://doi.org/10.1038/s41586-019-1923-7
6. A. Mirhoseini, A. Goldie, M. Yazgan, J.W. Jiang, E. Songhori, S. Wang, Y.J. Lee, E. Johnson, O. Pathak, A. Nazi, et al., Nature **594**(7862), 207 (2021). DOI https://doi.org/10.1038/s41586-021-03544-w
7. T.N. Theis, H.S.P. Wong, Computing in Science & Engineering **19**(2), 41 (2017). DOI 10.1109/MCSE.2017.29
8. C.E. Leiserson, N.C. Thompson, J.S. Emer, B.C. Kuszmaul, B.W. Lampson, D. Sanchez, T.B. Schardl, Science **368**(6495), eaam9744 (2020). DOI 10.1126/science.aam974
9. G. Wetzstein, A. Ozcan, S. Gigan, S. Fan, D. Englund, M. Soljačić, C. Denz, D.A. Miller, D. Psaltis, Nature **588**(7836), 39 (2020). DOI https://doi.org/10.1038/s41586-020-2973-6
10. Y. Shen, N.C. Harris, S. Skirlo, M. Prabhu, T. Baehr-Jones, M. Hochberg, X. Sun, S. Zhao, H. Larochelle, D. Englund, et al., Nat. Photonics **11**(7), 441 (2017). DOI https://doi.org/10.1038/nphoton.2017.93
11. N.C. Harris, J. Carolan, D. Bunandar, M. Prabhu, M. Hochberg, T. Baehr-Jones, M.L. Fanto, A.M. Smith, C.C. Tison, P.M. Alsing, et al., Optica **5**(12), 1623 (2018). DOI https://doi.org/10.1364/OPTICA.5.001623
12. Z. Ying, C. Feng, Z. Zhao, S. Dhar, H. Dalir, J. Gu, Y. Cheng, R. Soref, D.Z. Pan, R.T. Chen, Nat. Commun. **11**, 2154 (2020). DOI https://doi.org/10.1038/s41467-020-16057-3
13. H. Zhang, M. Gu, X. Jiang, J. Thompson, H. Cai, S. Paesani, R. Santagati, A. Laing, Y. Zhang, M. Yung, et al., Nat. Commun. **12**, 457 (2021). DOI https://doi.org/10.1038/s41467-020-20719-7
14. J. Feldmann, N. Youngblood, M. Karpov, H. Gehring, X. Li, M. Stappers, M. Le Gallo, X. Fu, A. Lukashchuk, A. Raja, et al., Nature **589**(7840), 52 (2021). DOI https://doi.org/10.1038/s41586-020-03070-1
15. X. Lin, Y. Rivenson, N.T. Yardimci, M. Veli, Y. Luo, M. Jarrahi, A. Ozcan, Science **361**(6406), 1004 (2018). DOI 10.1126/science.aat8084
16. Y. Luo, D. Mengu, N.T. Yardimci, Y. Rivenson, M. Veli, M. Jarrahi, A. Ozcan, Light: Science & Applications **8**(1), 1 (2019). DOI https://doi.org/10.1038/s41377-019-0223-1
17. D. Mengu, Y. Luo, Y. Rivenson, A. Ozcan, IEEE Journal of Selected Topics in Quantum Electronics **26**(1), 1 (2019). DOI 10.1109/JSTQE.2019.2921376
18. S. Jiao, J. Feng, Y. Gao, T. Lei, Z. Xie, X. Yuan, Opt. Lett. **44**(21), 5186 (2019). DOI https://doi.org/10.1364/OL.44.005186
19. R. Hamerly, L. Bernstein, A. Sludds, M. Soljačić, D. Englund, Phys. Rev. X **9**(2), 021032 (2019). DOI https://doi.org/10.1103/PhysRevX.9.021032
20. L. Mennel, J. Symonowicz, S. Wachter, D.K. Polyushkin, A.J. Molina-Mendoza, T. Mueller, Nature **579**(7797), 62 (2020). DOI https://doi.org/10.1038/s41586-020-2038-x
21. J. Spall, X. Guo, T.D. Barrett, A. Lvovsky, Opt. Lett. **45**(20), 5752 (2020). DOI https://doi.org/10.1364/OL.401675
22. L. Bernstein, A. Sludds, R. Hamerly, V. Sze, J. Emer, D. Englund, Sci. Rep. **11**, 3144 (2021). DOI https://doi.org/10.1038/s41598-021-82543-3
23. W. Gao, C. Yu, R. Chen, Advanced Photonics Research p. 2100048 (2021). DOI https://doi.org/10.1002/adpr.202100048

24. F. Léonard, A.S. Backer, E.J. Fuller, C. Teeter, C.M. Vineyard, ACS Photonics **8**(7), 2103 (2021). DOI https://doi.org/10.1021/acsphotonics.1c00526
25. F. Léonard, E.J. Fuller, C.M. Teeter, C.M. Vineyard, Opt. Express **30**(8), 12510 (2022). DOI https://doi.org/10.1364/OE.455007
26. T. Wang, S.Y. Ma, L.G. Wright, T. Onodera, B.C. Richard, P.L. McMahon, Nat. Commun. **13**, 123 (2022). DOI https://doi.org/10.1038/s41467-021-27774-8
27. H. Zeng, J. Fan, Y. Zhang, Y. Su, C. Qiu, W. Gao, Opt. Express **30**(8), 12712 (2022). DOI https://doi.org/10.1364/OE.453363
28. Y. Tang, P.T. Zamani, R. Chen, J. Ma, M. Qi, C. Yu, W. Gao, Laser Photonics Rev. p. 2200381 (2022). DOI https://doi.org/10.1002/lpor.202200381
29. D. Mengu, M.S.S. Rahman, Y. Luo, J. Li, O. Kulce, A. Ozcan, Adv. Opt. Photonics **14**(2), 209 (2022). DOI https://doi.org/10.1364/AOP.450345
30. T. Fu, Y. Zang, H. Huang, Z. Du, C. Hu, M. Chen, S. Yang, H. Chen, Opt. Express **29**(20), 31924 (2021). DOI https://doi.org/10.1364/OE.435183
31. Q. Song, X. Liu, C.W. Qiu, P. Genevet, Appl. Phys. Rev. **9**(1), 011311 (2022). DOI https://doi.org/10.1063/5.0078610
32. R. Rojas, in *Neural networks* (Springer, 1996), pp. 149–182. DOI https://doi.org/10.1007/978-3-642-61068-4_7
33. D. Mengu, Y. Rivenson, A. Ozcan, ACS Photonics **8**(1), 324 (2020). DOI https://doi.org/10.1021/acsphotonics.0c01583
34. D. Mengu, Y. Zhao, N.T. Yardimci, Y. Rivenson, M. Jarrahi, A. Ozcan, Nanophotonics **9**(13), 4207 (2020). DOI https://doi.org/10.1515/nanoph-2020-0291
35. Y. Li, Z. Zheng, R. Li, Q. Chen, H. Luan, H. Yang, Q. Zhang, M. Gu, Opt. Express **30**(20), 36700 (2022). DOI https://doi.org/10.1364/OE.468648
36. M. Tonouchi, Nat. Photonics **1**(2), 97 (2007). DOI https://doi.org/10.1038/nphoton.2007.3
37. S. Jahani, Z. Jacob, Nat. Nanotechnol. **11**(1), 23 (2016). DOI https://doi.org/10.1038/nnano.2015.304
38. H. Chen, J. Feng, M. Jiang, Y. Wang, J. Lin, J. Tan, P. Jin, Engineering **7**(10), 1483 (2021). DOI https://doi.org/10.1016/j.eng.2020.07.032
39. E. Goi, X. Chen, Q. Zhang, B.P. Cumming, S. Schoenhardt, H. Luan, M. Gu, Light Sci. Appl. **10**, 40 (2021). DOI https://doi.org/10.1038/s41377-021-00483-z
40. X. Luo, Y. Hu, X. Ou, X. Li, J. Lai, N. Liu, X. Cheng, A. Pan, H. Duan, Light Sci. Appl. **11**, 158 (2022). DOI https://doi.org/10.1038/s41377-022-00844-2
41. G. Zheng, H. Mühlenbernd, M. Kenney, G. Li, T. Zentgraf, S. Zhang, Nat. Nanotechnol. **10**(4), 308 (2015). DOI https://doi.org/10.1038/nnano.2015.2
42. A. Silva, F. Monticone, G. Castaldi, V. Galdi, A. Alù, N. Engheta, Science **343**(6167), 160 (2014). DOI 10.1126/science.1242818
43. L. Wan, D. Pan, T. Feng, W. Liu, A.A. Potapov, Front. Optoelectron. **14**(2), 187 (2021). DOI https://doi.org/10.1007/s12200-021-1124-5
44. J. Sol, D.R. Smith, P. Del Hougne, Nat. Commun. **13**, 1713 (2022). DOI https://doi.org/10.1038/s41467-022-29354-w
45. W. Fu, D. Zhao, Z. Li, S. Liu, C. Tian, K. Huang, Light Sci. Appl. **11**, 62 (2022). DOI https://doi.org/10.1038/s41377-022-00752-5
46. V. Mazzia, F. Salvetti, M. Chiaberge, Sci. Rep. **11**, 14634 (2021). DOI https://doi.org/10.1038/s41598-021-93977-0
47. J. Li, D. Mengu, Y. Luo, Y. Rivenson, A. Ozcan, Adv. Photon. **1**(4), 046001 (2019). DOI https://doi.org/10.1117/1.AP.1.4.046001
48. M.S.S. Rahman, J. Li, D. Mengu, Y. Rivenson, A. Ozcan, Light Sci. Appl. **10**, 14 (2021). DOI https://doi.org/10.1038/s41377-020-00446-w
49. Y. Li, R. Chen, B. Sensale-Rodriguez, W. Gao, C. Yu, Sci. Rep. **11**, 11013 (2021). DOI https://doi.org/10.1038/s41598-021-90221-7
50. J. Li, Y.C. Hung, O. Kulce, D. Mengu, A. Ozcan, Light Sci. Appl. **11**, 153 (2022). DOI https://doi.org/10.1038/s41377-022-00849-x
51. J. Li, D. Mengu, N.T. Yardimci, Y. Luo, X. Li, M. Veli, Y. Rivenson, M. Jarrahi, A. Ozcan, Sci. Adv. **7**(13), eabd7690 (2021). DOI 10.1126/sciadv.abd7690

52. S. Zarei, M.r. Marzban, A. Khavasi, Opt. Express **28**(24), 36668 (2020). DOI https://doi.org/10.1364/OE.404386
53. Z. Wang, L. Chang, F. Wang, T. Li, T. Gu, Nat. Commun. **13**, 2131 (2022). DOI https://doi.org/10.1038/s41467-022-29856-7
54. H. Zhu, J. Zou, H. Zhang, Y. Shi, S. Luo, N. Wang, H. Cai, L. Wan, B. Wang, X. Jiang, et al., Nat. Commun. **13**, 1044 (2022). DOI https://doi.org/10.1038/s41467-022-28702-0
55. L. Wu, Z. Zhang, Opt. Express **30**(15), 28024 (2022). DOI https://doi.org/10.1364/OE.462370
56. D. Pierangeli, G. Marcucci, C. Conti, Photonics Res. **9**(8), 1446 (2021). DOI https://doi.org/10.1364/PRJ.423531
57. M. Miscuglio, Z. Hu, S. Li, J.K. George, R. Capanna, H. Dalir, P.M. Bardet, P. Gupta, V.J. Sorger, Optica **7**(12), 1812 (2020). DOI https://doi.org/10.1364/OPTICA.408659
58. T. Zhou, X. Lin, J. Wu, Y. Chen, H. Xie, Y. Li, J. Fan, H. Wu, L. Fang, Q. Dai, Nat. Photonics **15**(5), 367 (2021). DOI https://doi.org/10.1038/s41566-021-00796-w
59. M. Lou, Y.L. Li, C. Yu, B. Sensale-Rodriguez, W. Gao, Opt. Lett. **48**(2), 219 (2023). DOI https://doi.org/10.1364/OL.477605
60. K. Makino, K. Kato, Y. Saito, P. Fons, A.V. Kolobov, J. Tominaga, T. Nakano, M. Nakajima, J. Mater. Chem. C. **7**(27), 8209 (2019). DOI https://doi.org/10.1039/C9TC01456J
61. M. Wuttig, H. Bhaskaran, T. Taubner, Nat. Photonics **11**(8), 465 (2017). DOI https://doi.org/10.1038/nphoton.2017.126
62. M. Mansouree, A. McClung, S. Samudrala, A. Arbabi, ACS Photonics **8**(2), 455 (2021). DOI https://doi.org/10.1021/acsphotonics.0c01058
63. L.G. Wright, T. Onodera, M.M. Stein, T. Wang, D.T. Schachter, Z. Hu, P.L. McMahon, Nature **601**(7894), 549 (2022). DOI https://doi.org/10.1038/s41586-021-04223-6
64. R. Chen, Y. Li, M. Lou, J. Fan, Y. Tang, B. Sensale-Rodriguez, C. Yu, W. Gao, Laser Photonics Rev. p. 2200348 (2022). DOI https://doi.org/10.1002/lpor.202200348
65. G. Vdovin, H. van Brug, F. van Goor, in *Fifth International Topical Meeting on Education and Training in Optics, Delft, The Netherlands* (1997), pp. 19–21. DOI https://doi.org/10.1117/12.294366